Machine Learning-Driven Joint Structuring of WPT Coil and Core for Enhanced Mutual Inductance and Reduced Ferrite Volume

Fawad, Syed Ahson Ali Shah, *Member, IEEE*, Yohan Park, *Student Member, IEEE*, and Yun-Su Kim, *Senior Member, IEEE*

***Abstract*—Machine learning (ML) algorithms have shown promise in optimizing wireless power transfer (WPT) systems, particularly for electric vehicle charging and medical implants. However, most approaches focus on isolated WPT components, limiting their overall impact. This study presents an integrated optimization of WPT coil and core designs to enhance mutual inductance between transmitting (Tx) and receiving (Rx) coils. We propose a hybrid residual layer sequential neural network (HRL-SeqNet), along with SVR-based multivariate regression and deep Q-network (DQN) models, to enhance the WPT performance. HRL-SeqNet incorporates GRU, BiLSTM, and LSTM RNNs followed by a second-level GRU and ensemble regression to optimize the copper windings, achieving a high mutual inductance of 11.284 μH with a conventional ferrite core. In addition, SVR and DQN models optimize the ferrite core by introducing asymmetric and symmetric vacuum configurations. The SVR-optimized asymmetric core achieved a 0.585% increase in mutual inductance while reducing ferrite volume by 24.49%. In addition, the DQN model increased mutual inductance by 1.38% and 3.16% for order 4 and order 8 rotational symmetry, respectively, with corresponding reductions in ferrite volume of 23.47% and 25.51%. These ML models show exceptional computational efficiency, with HRL-SeqNet, SVR, and DQN achieving 4,300x, 16,960x, and 10,138x speedups, respectively, over ANSYS Maxwell simulations. Experimental validations confirm the effectiveness of these ML-optimized designs, demonstrating their applicability across various WPT applications.**

***Index Terms*—Artificial intelligence, electroceuticals, healthcare, inductive power transfer, machine learning (ML).**

I. Introduction

WIRELESS power transfer (WPT) has attracted substantial interest for developing and miniaturizing implantable medical devices used in biomedical and industrial applications. Implantable medical devices include endoscopic capsules, artificial hearts, artificial retinal prostheses, and electrical stimulators [1], [2], [3]. Traditionally implantable medical devices have been either powered by implantable batteries or percutaneous cables [4]. However, the use of cables increases the risk of infection, while batteries have a limited service life, add to the volume and weight of devices, and require frequent surgical replacements. To address existing power delivery limitations in implantable medical devices, WPT systems based on inductive power transfer are being developed to facilitate wireless energy transfer from an external source to an implanted device, thereby eliminating the need for physical connections. Structure optimization of WPT components is crucial for achieving high mutual inductance (MI) between coupling coils, but separately optimizing individual components does not yield the best results. Coil design [5], core design [6], and automatic impedance matching [7] have been optimized separately, neglecting other components. Optimizing the design of WPT coils and ferrite cores can enhance power efficiency, but their combined geometry has often been overlooked despite its importance in WPT systems. The optimal core not only reduces the volume, weight, and cost of WPT in implantable medical devices but may also enhance the power efficiency of the WPT system. The design of ferrite core layouts within WPT systems has generally relied on intuition and iterative simulation analysis [8]. On the other hand, theoretical analysis using electromagnetic theory has been limited by the nonlinear magnetic field distortion from ferrite cores [9]. Consequently, previous studies have largely relied on simulation analysis or empirical equations to understand the magnetic field distribution caused by the ferrite core. Recognizing the limitations of conventional theoretical and simulation-based methods, we introduce a machine learning (ML) approach for structural design optimization, as given in Fig. 1.

ML methods are broadly categorized into those based on handcrafted features and feature learning (FL) methods. FL-based methods include convolutional neural networks (CNNs) and deep neural networks (DNNs) for classifying, regression, or reinforcement learning (RL). While handcrafted-feature-based methods target specific data characteristics, they often overlook others. In contrast, FL-based methods depend on the quality of the training data and include RL, which learns optimal actions through trial and error to maximize the expected rewards. Methods based on handcrafted features include the support vector machine (SVM), k-nearest neighbors algorithm,

Received 12 December 2024; revised 22 February 2025 and 7 April 2025; accepted 14 May 2025. Date of publication 22 May 2025; date of current version 5 August 2025. This work was supported in part by the National Research Foundation of Korea (NRF) under Grant RS-2024-00427153 and in part by the Korea government (MSIT). Recommended for publication by Associate Editor C. K. Lee. *(Corresponding author: Yun-Su Kim.)*

The authors are with the Department of Electrical Engineering and Computer Science, Gwangju Institute of Science and Technology, Gwangju 61005, South Korea (e-mail: fawad7528@gist.ac.kr; sahsonas@gist.ac.kr; yohanpark@gm.gist.ac.kr; yunsukim@gist.ac.kr).

Color versions of one or more figures in this article are available at https://doi.org/10.1109/TPEL.2025.3571751.

Digital Object Identifier 10.1109/TPEL.2025.3571751

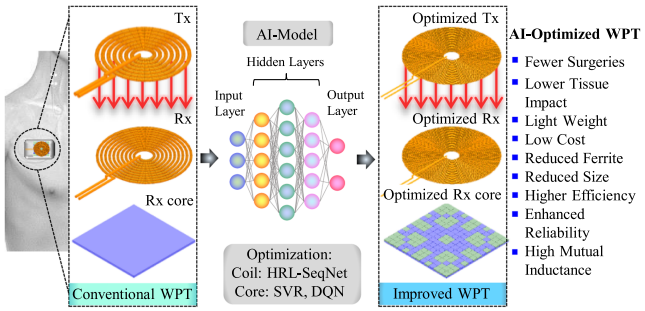

Fig. 1. Generalized framework showing the flow from raw WPT design input to the AI model, leading to the optimization of the WPT coil and core structure.

and decision trees, but they struggle to scale to large datasets, whereas FL-based methods may efficiently manage scalability and complex WPT data patterns [10], [11]. Ensemble techniques are often used to optimally combine feature descriptors, thereby enhancing the robustness and invariance of feature vectors [12]. Given the diverse coil and core geometries of WPT systems and minimal interclass variations across patterns, ensemble methods can improve the design performance.

Computational intelligence techniques, such as artificial neural networks (ANNs), swarm intelligence, and evolutionary computation (e.g., genetic algorithms—GAs and particle swarm optimization—PSO), are commonly adopted for WPT optimization [13]. PSO and GAs iterate over a group of generations searching for an optimal result, but PSO does not use evolutionary operators like crossover and mutation in GAs. Instead, PSO particles move through the problem space by following the current optimal particles. In contrast, ANNs adjust weights between neurons during learning, effectively solving complex nonlinear problems and being widely used for tasks such as adaptive control and function approximation due to their ability to handle imprecise data and perform nonlinear mapping [14]. ANN-based WPT optimization focuses on increasing the power transfer efficiency (PTE), and the corresponding ANNs are typically validated by comparing its results with those obtained from finite element analysis (FEA) using software, such as ANSYS Maxwell.

CNNs and DNNs have gained popularity in ML-based optimization [10]. To reduce the core volume and magnetic loss for multiobjective optimization in WPT, a GA was employed with a trained ANN to establish the fitness function, thus replacing FEA for fast optimization [15]. Combining an ANN with FEA as a fitness function accelerates optimization, but the optimization accuracy depends largely on the ANN training performance. In [16], GAs were used to optimize the ANN weights for improving the training quality. In [17], an RL algorithm was employed to optimize the ferromagnetic core geometry for higher coupling between the transmitter (Tx) and receiver (Rx) coils at 98 cm in a WPT system. In [18], RL was combined with ϵ-greedy Q-learning, increasing the MI by 2% while reducing the computation time by 50%. While RL reduces the computational burden, learning often converges to a local optimum rather than the global optimum. For WPT, a comprehensive survey was conducted for supervised and unsupervised learning, including CNNs, deep belief networks, autoencoder networks, recurrent neural networks, deep RL networks, and generative adversarial networks, as well as their advantages and drawbacks [19]. CNNs mostly suffer from low accuracy and high computational cost [20], while autoencoder networks fail when the data strength is large [21]. Deep belief networks require sophisticated hardware [22], and recurrent neural networks become more complex as the data volume to be processed increases [23]. RL suffers from low sample efficiency [24], while generative adversarial networks suffer from training instability [25]. Considering the characteristics of various ML algorithms, we developed a hybrid and residual supervised network combining gate recurrent units (GRUs), long short-term memory (LSTM), and the bidirectional LSTM (BiLSTM) architecture [26].

The proposed ML algorithm is trained on simulated data from the Ansys Maxwell FEA tool to estimate the geometry of the copper coil and ferrite core that maximizes the MI between the Tx and Rx coils in a WPT system for electroceutical devices. The proposed framework optimizes the WPT coil and core to enhance the MI and reduce the ferrite required in the Rx system. The key contributions of this study are summarized as follows:

1) We introduce a hybrid and residual-layer-based sequential neural network (HRL-SeqNet) that consists of four blocks built with GRU, LSTM, and BiLSTM layers, along with rectified linear unit (ReLU), normalization, and dropout layers for robustness. The proposed model incorporates skip connections that bypass previous blocks, feeding stronger features into subsequent cascaded layers and preventing the vanishing gradient problem.
2) Extensive simulations were performed to iteratively optimize the neural block composition of HRL-SeqNet. Optimization included determining the number of hidden units, dropout size, and training parameters (e.g., learning rate and epoch size) through parametric analysis. The HRL-SeqNet DNN was intended to optimize the coil geometry for efficient MI between Tx and Rx WPT coils with similar parameters.
3) We utilized support vector regression (SVR) and a deep Q-network (DQN) to optimize the Rx ferrite core, with SVR yielding an asymmetric structure and DQN producing fourth- and eighth-order rotationally symmetric structures.

The rest of this article is organized as follows. Section II describes the proposed method, while Section III presents evaluation results, and Section IV covers experimental verification. Finally, Section V concludes this article.

II. Methods

The proposed ML-based optimization of WPT components focuses on the coil and ferrite core geometry, and it consists of two stages. In the first stage, the planar spiral Tx and Rx coil geometry is optimized through the proposed HRL-SeqNet for the solid ferrite core. This involves identifying geometric parameters such as the wire thickness, inner radius, radius change, and number of turns that maximize the MI between the coils. In the second stage, the optimized coil obtained in the first stage

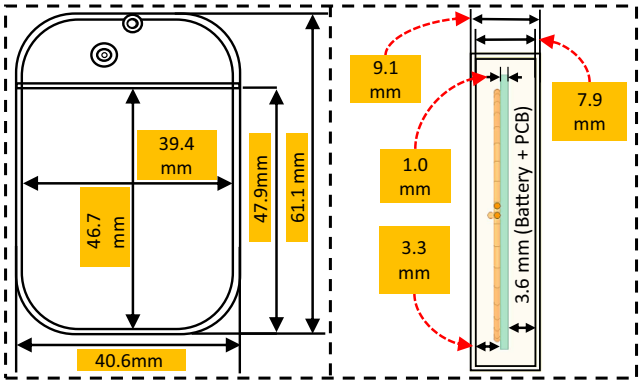

Fig. 2. Top and side views of implantable device casing.

is utilized, and the ferrite core structure is further optimized by employing the SVR and DQN models to reduce the ferrite core volume such that WPT increases the MI.

A. Degrees of Freedom and Design Space

We miniaturize an implantable electroceutical device by incorporating space for a rechargeable battery, printed circuit board (PCB), and Rx of the WPT system, as well as optimizing the WPT components, including the coils and cores, as shown in Fig. 2. The total inner space for the battery, PCB, and WPT Rx coil components is 4.3 mm, with 3.6 mm allocated to the battery and PCB. The core and coil share a $35 \times 35 \times 4.3$ mm volume, with 1 mm for the core and 3.3 mm for the coil. The Rx coil is designed in a spiral planar configuration, with a feeding wire of similar thickness. Based on the available space and market availability of copper wires, thicknesses ranging from 0.1 to 1.6 mm, except for 0.9 mm, are available. Considering all combinations of wire thicknesses, turn counts, inner radii, and spacings, 322 172 valid coils are obtained. With each Ansys Maxwell simulation taking 10 min, simulating all cases would take six years, making ML essential for optimizing the coil parameters in reasonable time.

B. Coil Optimization

The WPT coil optimization framework described in Algorithm 1 clusters input parameters X into k groups using K means, obtaining corresponding MI values M_k through Ansys simulations to train the HRL-SeqNet model. This process involves iteratively refining the training data based on feedback from Ansys, with centroids and their rewards serving as inputs to ensure uniformity and reduce bias. The algorithm continues until the iteration limit $\mathcal{L}$ is reached, then providing optimal input parameters X_o that correspond to the highest estimated MI, M_{Est}. During each iteration, the model estimates rewards for all test cases, simulating those with high MI in Ansys for validation. The top N cases from the Ansys results are then added to training dataset D_{tr}. Over $\mathcal{L}$ iterations, this refinement leads to the selection of the optimal coil structure. The trained HRL-SeqNet estimates reward values for all test samples, with the highest MI sample considered as the optimal coil structure.

Algorithm 1: Coil Optimization Framework.

Input: HRL-SeqNet, iteration limit $\mathcal{L}$, clusters k, and input parameters X
Output: Optimal input parameter X_o
Clustering: $C_{\mathbf{k}} = \mathbf{KMeans}(X, k)$
Train data $D_{\mathbf{tr}} : [C_k, M_k]_{i=1}^{k} \leftarrow M_k = \mathbf{Ansys}(C_k)$
while $i < \mathcal{L}$ **do**
  $M_{\mathbf{Est}} = \mathbf{HRL\text{-}SeqNet}(X)$ after training on $D_{\mathbf{tr}}$
  $D'_{\text{tr}} \leftarrow \{(X^i, M^i_{\text{Est}}) \mid i \in [1, n], \forall j < i,\ M^i_{\text{Est}} > M^j_{\text{Est}}\}$
  $X_s \leftarrow \{(X^i, M^i_{\text{Est}}) \in D'_{\text{tr}} \mid i \in [1, N]\}$
  $M_s = \mathbf{Ansys}(X_s)$
  $D_{\text{tr}} \leftarrow D_{\text{tr}} \cup \{(X_s, M_s)\}$
end while
$X_o \leftarrow X^{i^*}$, where $i^* = \arg\max_{(X^j, M^j_{\text{Est}})} M^j_{\text{Est}}$

1) HRL-SeqNet: The proposed HRL-SeqNet architecture comprises three parallel sequential DNN blocks cascaded into a single sequential DNN block and followed by an ensemble classifier. In the WPT system, unlike other dense layers, the GRU, LSTM, and BiLSTM layers capture the complex nonlinear interactions among coil design parameters, optimizing the MI. Therefore, these layers constitute the first stage of our model. For fine-tuning, we use a cascaded GRU in the second stage. The input training data are first fed to the three sequential DNN blocks for feature extraction, as illustrated in Fig. 3. Each sequential block comprises six layers: a sequential ANN, batch normalization, dropout, ReLU, fully connected (FC), and regression layers. The three sequential blocks are GRU, BiLSTM, and LSTM blocks. The GRU layer consists of $\mathcal{N}$ GRU cells ($\mathcal{N} = 8$ in this study), each with update and reset gates. In the first phase, the $\mathcal{N}$th unit cell of the GRU block has $\mathbf{X}_t$ and $\mathbf{Y}^g_t$ as its input and output at timestamp t, respectively. The GRU for the $\mathcal{N}$th GRU cell is formulated as follows:

$$\mathbf{Y}^g_t = (1 - \boldsymbol{\zeta}_t) \odot \mathbf{Y}^g_{t-1} + \boldsymbol{\zeta}_t \odot \tilde{\mathbf{Y}}^g_t \tag{1}$$

$$\tilde{\mathbf{Y}}^g_t = \tanh\left(\mathcal{W}_h \cdot \left[\sigma\left(\mathcal{W}_\rho \cdot \left[\mathbf{Y}^g_{t-1}, \mathbf{X}_t\right] + \Psi_\rho\right) \odot \mathbf{Y}^g_{t-1}\right]\right) + \Psi_h \tag{2}$$

$$\boldsymbol{\zeta}_t = \sigma\left(\mathcal{W}_\zeta \cdot \left[\mathbf{Y}^g_{t-1}, \mathbf{X}_t\right] + \Psi^\zeta\right) \tag{3}$$

$\boldsymbol{\zeta}_t$ in (1) is the update gate value at time t, $\odot$ denotes elementwise multiplication, $\tilde{\mathbf{Y}}^g_t$ is the hidden state of the GRU at time t, $\mathcal{W}_h$, $\mathcal{W}_\rho$, and $\mathcal{W}_\zeta$ are the weight matrices for the candidate hidden state, reset gate, and update gate, respectively, Ψ_h, Ψ_ρ, and Ψ^ζ are bias vectors for the candidate hidden state, reset gate, and update gate, respectively, and activation function $\sigma(x) = (1 + e^{-x})^{-1}$ maps input values between 0 and 1, controlling the update and reset gates.

The third LSTM block in the sequential DNN extracts features from input $\mathbf{X}_t$. This block is formulated as follows:

$$i_t = \sigma(\mathcal{W}_{xi}\mathbf{X}_t + \mathcal{W}_{\mathcal{F}i}\mathcal{F}_{t-1} + \Psi_i)$$
$$f_t = \sigma(\mathcal{W}_{xf}\mathbf{X}_t + \mathcal{W}_{\mathcal{F}f}\mathcal{F}_{t-1} + \Psi_f)$$
$$o_t = \sigma(\mathcal{W}_{xo}\mathbf{X}_t + \mathcal{W}_{\mathcal{F}o}\mathcal{F}_{t-1} + \Psi_o)$$

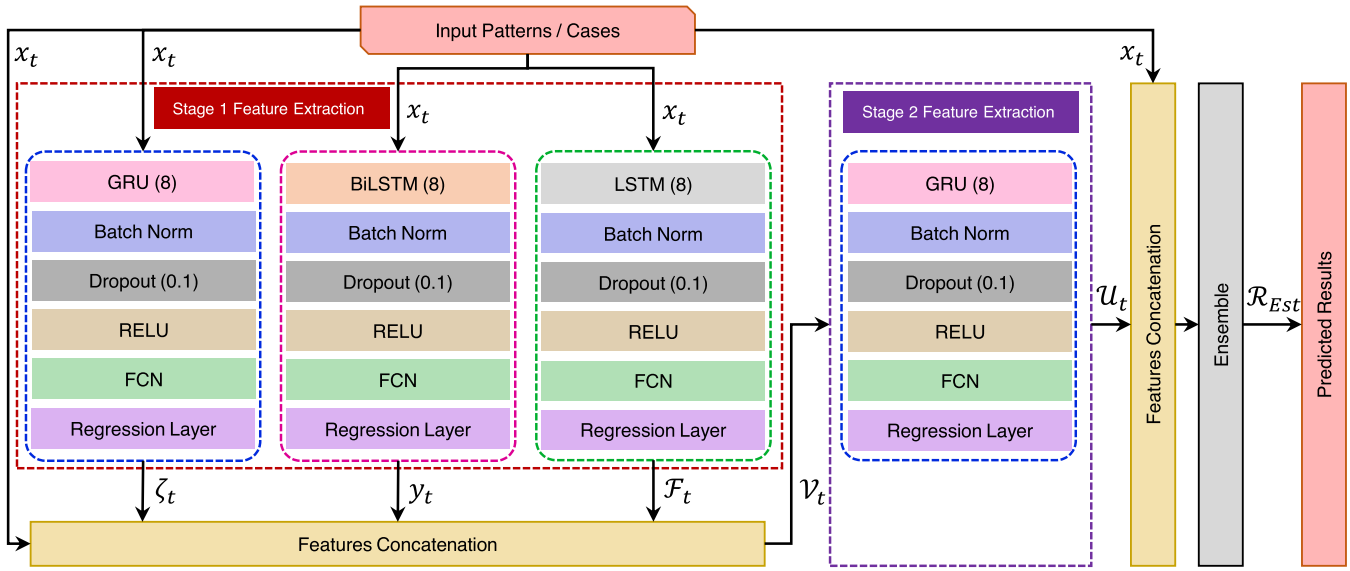

Fig. 3. Proposed HRL-SeqNet based on hybrid and residual layers for enhanced optimization of WPT coil and core design.

$$\tilde{c}_t = \tanh(\mathcal{W}_{xc}\mathbf{X}_t + \mathcal{W}_{\mathcal{F}c}\mathcal{F}_{t-1} + \Psi_c)$$
$$c_t = f_t \odot c_{t-1} + i_t \odot \tilde{c}_t$$
$$\mathcal{F}_t = o_t \odot \tanh(c_t) \tag{4}$$

where $\mathbf{X}_t$ is the input vector at timestep t, $\mathcal{F}_{t-1}$ is the hidden state from the previous timestep, $\mathcal{W}_{xi}$, $\mathcal{W}_{xf}$, $\mathcal{W}_{xo}$, and $\mathcal{W}_{xc}$ are the weight matrices for the input connections, $\mathcal{W}_{\mathcal{F}i}$, $\mathcal{W}_{\mathcal{F}f}$, $\mathcal{W}_{\mathcal{F}o}$, and $\mathcal{W}_{\mathcal{F}c}$ are the weight matrices for the hidden state connections, Ψ_i, Ψ_f, Ψ_o, and Ψ_c are the bias vectors, σ is the sigmoid activation function, $\tanh$ is the hyperbolic tangent activation function, and $\odot$ denotes elementwise multiplication.

The BiLSTM block contains eight hidden units and is used in the first stage of HRL-SeqNet for feature extraction. It processes input $\mathbf{X}_t$ at timestep t using forward and backward LSTM, producing output $\mathbf{Y}_t$. Each unit cell of the BiLSTM block processes the input data sequentially and captures temporal dependencies bidirectionally. In BiLSTM, the forgetting gate initially computes forgetting factor f_t considering previous cell state c_{t-1}. Then, the input gate determines the new information to update in the cell state using input variables $\mathbf{X}_t$ and $\mathbf{Y}_{t-1}$, creating candidate state $\tilde{c}_t$ through the hyperbolic tangent function. The input and forget gates control information preservation and forgetting, respectively, establishing a new cell state, c_t. Finally, the output gate determines part of output information o_t using sigmoid activation, which is then combined with new cell state c_t to produce the output. Output $\mathbf{Y}_t$ can be expressed as follows:

$$\vec{\mathbf{Y}}_t = \mathcal{L}_f(\mathbf{X}_t, \mathbf{Y}_{t-1}) \tag{5}$$
$$\acute{\mathbf{Y}}_t = \mathcal{L}_b(\mathbf{X}_t, \acute{\mathbf{Y}}_{t+1}) \tag{6}$$

where $\mathbf{Y}_t$ is the concatenated output of forward LSTM $\mathcal{L}_f$ and backward LSTM $\mathcal{L}_b$, $\mathcal{L}_f$ represents forward LSTM, which processes input $\mathbf{X}_t$ and previous hidden state $\mathbf{Y}_{t-1}$, producing output $\vec{\mathbf{Y}}_t$, and $\mathcal{L}_b$ represents backward LSTM, which processes input $\mathbf{X}_t$ and next hidden state $\acute{\mathbf{Y}}_{t+1}$, producing output $\acute{\mathbf{Y}}_t$. The overall output, $\mathbf{Y}_t$, is obtained by concatenating these two outputs as follows:

$$\mathbf{Y}_t = [\vec{\mathbf{Y}}_t, \acute{\mathbf{Y}}_t]. \tag{7}$$

The concatenation of feature vectors obtained from $\mathbf{X}_t$ in the first stage is given by the GRU, BiLSTM, and LSTM blocks as ζ_t, $\mathbf{Y}_t$, and $\mathcal{F}_t$, respectively, and stored in $\mathcal{V}$. $\mathcal{V}$ also includes $\mathbf{X}_t$ through a skipping connection. Hence, $\mathcal{V}$ can be expressed as follows:

$$\mathcal{V}_t = [\zeta_t, \mathbf{Y}_t, \mathcal{F}_t, \mathbf{X}_t] \tag{8}$$

where $[\cdot]$ denotes concatenation. $\mathcal{V}$ concatenates all the features of the first stage, which are fed to the GRU in the second stage. Let the GRU in the second stage be denoted as $\mathcal{G}$ and its input and output at timestep t be $\mathcal{V}_t$ and $\mathcal{T}_t$, respectively. Then, $\mathcal{T}_t = \mathcal{G}(\mathcal{V}_t)$. ζ_t, $\mathbf{Y}_t$, $\mathcal{F}_t$, $\mathbf{X}_t$, and $\mathcal{T}_t$ are concatenated to constitute final feature vector $\mathcal{U}_t$

$$\mathcal{U}_t = [\zeta_t, \mathbf{Y}_t, \mathcal{F}_t, \mathbf{X}_t, \mathcal{T}_t]. \tag{9}$$

$\mathcal{U}_t$ contains a highly robust and distinctive feature set that minimizes the mean square error (MSE) in prediction when using an ensemble regressor. The ensemble layer performs regression to estimate the MI. The estimated reward is the MI for each coil structure, which is expressed as $\mathcal{R}_{\text{Est}}$. The ensemble regressor uses multiple regression through bagging with a decision tree learner. Bagging is a statistical technique known as bootstrap aggregation, where multiple subsets are generated from the training dataset through the sample with a replacement method. It is expressed as

$$M_{\text{Est}} = \frac{1}{M}\sum_{m=1}^{R} f_m(\mathcal{U}) \tag{10}$$

where R is the number of bootstrap learners. We set $R = 100$ corresponding to the decision tree learners. HRL-SeqNet estimates the MI represented as M_{Est}, and it is compared with

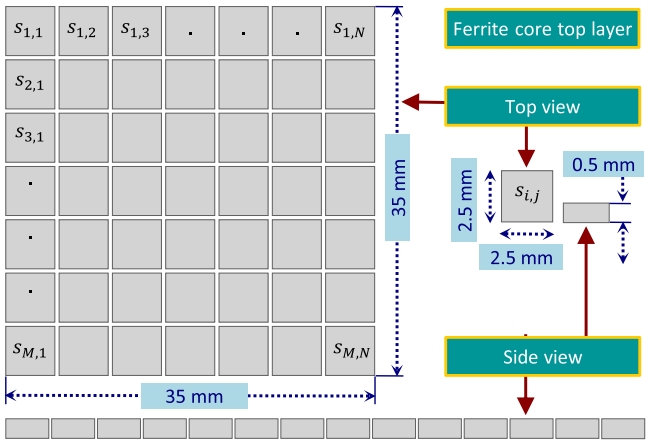

Fig. 4. Core diagram and dimensions.

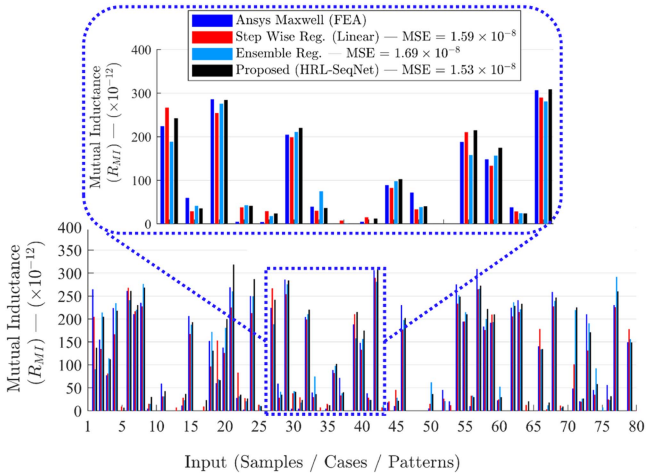

Fig. 5. MIs obtained from ANSYS, regression models, and proposed method.

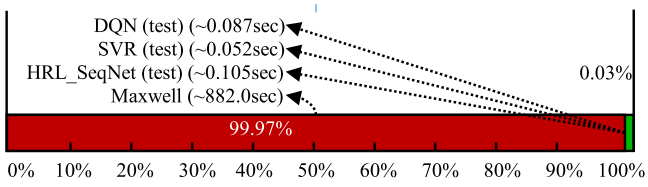

Fig. 6. Computation times for Ansys Maxwell simulation and ML models.

simulation results obtained from Ansys as ground truths to determine the MSE of the proposed model.

C. Core Optimization

1) SVR Optimization: For core structure optimization, the core is split into two layers, each with dimensions of $35 \times 35 \times 0.5$ mm. The upper layer is optimized by reducing ferrite and introducing vacuum patches. Each patch has dimensions of $2.5 \times 2.5 \times 0.5$ mm (length $\times$ width $\times$ thickness). The upper layer turns into a grid of dimensions 14×14, with each grid cell consisting of a patch. The lower layer of the ferrite core is kept solid to support the ferrite patches in the upper layer and maintain a realistic design. The MI corresponding to each patch within the grid is determined using Ansys through FEA. The patches producing MI higher than specified thresholds are assigned ferrite properties, while the remaining patches are assigned vacuum properties. The thresholds are determined through SVR. Each threshold $\gamma^{(k)}$ produces a different ferrite core geometry. Each patch is represented by $S_{i,j}$, with subscripts i and j representing the position coordinates within the grid, as illustrated in Fig. 4. $\mathcal{K}$ training samples are provided to the SVR model for estimating the optimal threshold $\gamma^{(k)}$ that results in higher MI $\mathcal{R}^{(k)}$. The objective function for SVR is given by

$$\min_{f,\upsilon_k,\upsilon_k^*} \frac{1}{2}\|f(\gamma^{(k)}) - \mathcal{R}^{(k)}\|^2 + C\sum_{k=1}^{\mathcal{K}}(\upsilon_k + \upsilon_k^*) \tag{11}$$

$$f(\gamma^{(k)}) - \mathcal{R}^{(k)} \leq \epsilon + \upsilon_k \tag{12}$$

$$\mathcal{R}^{(k)} - f(\gamma^{(k)}) \leq \epsilon + \upsilon_k^* \tag{13}$$

$$\upsilon_k, \upsilon_k^* \geq 0 \quad \text{for } k = 1, 2, \ldots, \mathcal{K} \tag{14}$$

where $f(\gamma^{(k)})$ is the SVR learning function, C is a regularization parameter, ϵ is a tradeoff variable, and υ_k and υ_k^* measure the deviation of the predicted output from the actual output for the kth training sample.

2) DQN Optimization: The core structure optimized with DQN consists of a four-layer ANN that approximates Q-value function $Q(p, a)$ given in (15). The network takes pattern p as input and estimates reward M_{Est} for each input. The four-layer configuration includes n hidden units in the first layer, followed by a layer with $\frac{n}{2}$ hidden units, using ReLU activation and a dropout rate of 0.2 to prevent overfitting. The final layer produces a single reward representing the Q-value for the given action.

$$Q(p,a) \leftarrow Q(p,a) + \alpha\left(M_{\text{Est}} + \gamma \max_{a'} Q(p',a')\right) - Q(p,a) \tag{15}$$

where a denotes the action, M_{Est} is the estimated MI, α is the learning rate, and γ is the discount factor. The loss function for the network is given by

$$L(\theta) = \mathbb{E}_{(p,a,M_{\text{Est}},p')\sim D}\left[\left(M_{\text{Est}} + \gamma \max_{a'} Q(p',a';\theta^-) - Q(p,a;\theta)\right)^2\right] \tag{16}$$

where $\mathbb{E}$ denotes the expected value over experience replay memory buffer D, which is used to train the ANN, and θ represents the ANN parameters. The prime symbol denotes the next value of each variable in iteration.

III. Results and Discussion

The performance of HRL-SeqNet for coil design was analyzed and compared with that of recently developed regression networks. In addition, the performance of the SVR/DQN-optimized core was compared with that of a conventional core. The simulation time comparison in Fig. 6 shows that HRL-SeqNet is 4300 times faster than ANSYS for reward estimation per input coil parameter. For core reward parameter estimation,

SVR is 16 960 times faster, while DQN is 10 138 times faster than the corresponding ANSYS Maxwell simulations. The simulation takes approximately 882 s per run with a medium mesh structure in a computer equipped with an Intel(R) Core(TM) i7-10700 processor at 2.90 GHz with 32 GB random access memory.

A. HRL-SeqNet Optimization Performance

The proposed HRL-SeqNet consists of four ANN blocks organized in two stages along with an ensemble regression layer. Each block includes a sequential network, batch normalization, dropout layer (set to 0.1), ReLU activation, fully connected network (FCN), and regression layer. Each sequential layer contains eight hidden units to prevent overfitting and both vanishing and exploding gradients. The ReLU in each layer removes nonlinearity, while the FCN aggregates the features. Each HRL-SeqNet block serves as a feature extractor, with the extracted values concatenated for ensemble regression. The neural layer parameters and layer configurations are adjusted to enhance the robustness of the extracted features. The key model parameters include eight hidden units in the recurrent layers, a dropout rate of 0.1, and batch normalization for training stability. The training parameters, such as learning rate of 0.01, mini-batch size of 32, and a maximum epoch count of 270, are optimized for efficient convergence using the stochastic gradient descent with momentum optimizer. These are aligned with physical constraints by training on coil geometry and MI values to ensure the optimization of both inductive properties and geometric factors.

Of 322 172 possible coil structures, HRL-SeqNet is only trained for 400 uniformly distributed samples, that is, 0.124% of the total number of samples. The training samples are selected through k-nearest neighbors clustering. The test accuracy of the proposed HRL-SeqNet is measured using the MSE. The MSE is determined for the estimated rewards of HRL-SeqNet and those obtained from Ansys Maxwell for the same input test samples. The MSE can validate the network layer configuration and parameter selection. Comparing the MSE of the proposed HRL-SeqNet with that of other regression models, our proposal has the best MSE with more precise rewards closer to the Ansys results. We randomly selected 100 samples from the test data for MSE calculation. Table I lists the performance of HRL-SeqNet and similar methods. The proposed HRL-SeqNet achieves the lowest MSE of 1.53×10^{-8} for MI. The training loss and root MSE for all the network layers are shown in Fig. 8 and demonstrate the effectiveness of the network training, as both metrics converge toward an optimal set of parameters.

Fig. 5 shows the MI results for 16 cases and the Ansys FEA results as a reference for the best-performing methods including our proposal. The stepwise and ensemble regression methods are included owing to their MSE values listed in Table I. The proposed HRL-SeqNet provides similar results to the Ansys Maxwell simulation regarding the estimated MI. The second-best method is the stepwise method, followed by ensemble regression. Fig. 7 shows the MI and magnetic flux for the 322 172 valid coil structures estimated by HRL-SeqNet.

TABLE I
MSE VALUES FOR MI ($\mathcal{R}_{\text{MI}}$) COMPARING HRL-SEQNET WITH VARIOUS REGRESSION MODELS

Method	Kernel	MSE ($\mathcal{R}_{\text{MI}}$)
Linear regression	Linear	1.65×10^{-8}
SVM regression	Linear	2.23×10^{-8}
SVM regression	Gaussian	1.84×10^{-8}
Gaussian process regression	Gaussian	4.45×10^{-8}
Stepwise linear regression	Linear	1.59×10^{-8}
Ensemble regression	–	1.69×10^{-8}
SVM regression	Quadratic	1.58×10^{-8}
ANN (L10) regression	–	1.83×10^{-8}
Multilayer perceptron regression	–	2.33×10^{-8}
GRU	–	1.99×10^{-8}
LSTM	–	1.88×10^{-8}
GRU · BiLSTM	–	1.98×10^{-8}
GRU · BiLSTM · LSTM	–	2.10×10^{-8}
GRU · BiLSTM · LSTM · FC1	–	3.65×10^{-8}
((GRU)||X) · BiLSTM · LSTM · FC1 · FC2 · FC3	–	1.54×10^{-8}
((GRU)||X) · BiLSTM · LSTM · FC1	–	1.55×10^{-8}
GRU · BiLSTM · LSTM · FC1 · FC2	–	4.24×10^{-8}
GRU · FC1 · FC2	–	2.53×10^{-8}
Proposed HRL-SeqNet	–	1.53×10^{-8}

(·, cascaded connection; ||, parallel connection)

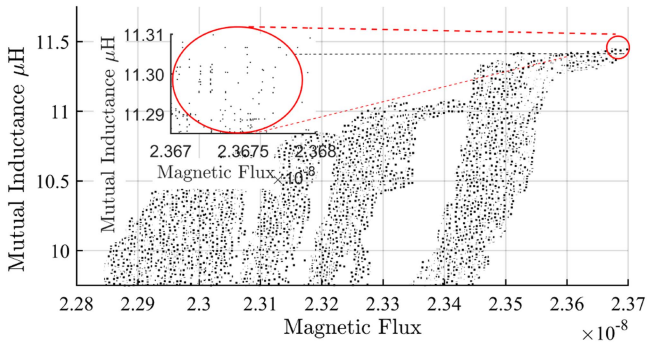

Fig. 7. MI versus magnetic flux leakage for all valid patterns, ensuring compliance with FDA limits.

TABLE II
OPTIMUM COIL GEOMETRIES AND MI ($\mathcal{R}_{MI}$) OF TX AND RX COILS OBTAINED FROM PROPOSED HRL-SEQNET

Wire radius	Initial radius	Radius change	No. turns	MI
0.225 mm	2.7 mm	0.49 mm	30	11.395 μH

TABLE III
SIMULATION RESULTS OF SVR AND DQN MODELS

Method	Core type	L_{Tx} (μH)	L_{Rx} (μH)	M (μH)
–	Conventional	16.48	26.26	11.39
SVR	Asymmetric	16.47	25.49	11.41
DQN	Order 4	16.54	25.53	11.60
DQN	Order 8	16.70	25.71	12.01

All magnetic flux results are under the FDA limit of 27μT, allowing to select the sample with the highest MI enclosed in a red circle [27]. Table II lists the Ansys Maxwell results for the best sample highlighted in Fig. 7. The optimal coil structure for an electroceutical device has 0.225 mm in wire thickness, 2.7 mm in initial radius, 0.49 mm in radius change, and 30 turns,

TABLE IV
COMPARISON OF THE FERRITE REDUCTION AND MI ENHANCEMENT FOR PATTERNS GENERATED WITH THE PROPOSED APPROACH COMPARED WITH CONVENTIONAL AND LITERATURE WORKS

Method/pattern	Conventional Full core	[28] Hybrid magnetic core	[6] DNN + Survival of fittest	Proposed Asymmetric (Fig. 9)	Proposed Symmetric order 4 (Fig. 9)	Proposed Symmetric order 8 (Fig. 9)
Ferrite reduction	0%	7.0%	10%	24.49%	23.47%	25.51%
MI	11.284 μH	—	—	11.350 μH	11.440 μH	11.640 μH
Increase	0%	0%	0.60%	0.585%	1.382%	3.1554%

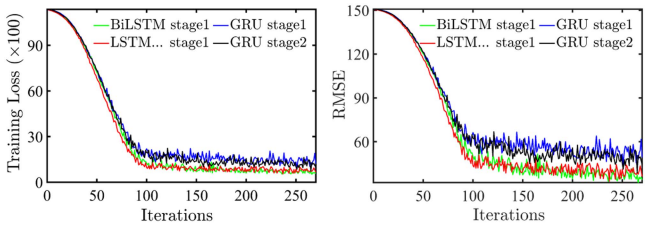

Fig. 8. Training loss and root MSE per iteration for sequential blocks in HRL-SeqNet.

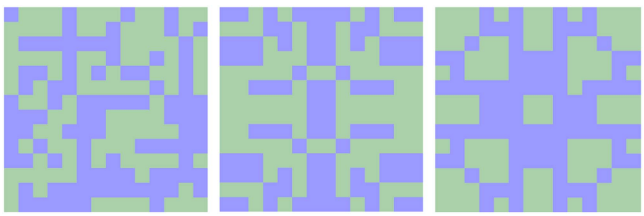

Fig. 9. Simulated core asymmetric (left) and symmetric cores with orders of four (middle) and eight (right).

yielding a maximum MI of 11.395 μH according to the Ansys Maxwell simulation results.

B. SVR Optimization Performance

The ferrite core with size of 35 × 35 × 1 mm is split into upper and lower layers with thickness 0.5 mm per layer. The upper layer is subjected to SVR optimization. In the first step, the cores are split into a grid of dimension 14 × 14 mm with every grid patch of 2.5 × 2.5 × 0.5 mm. Anys Maxwell FEA provides the MI considering one patch as ferrite and the remaining patches of the grid as vacuum. A total of 14 × 14 = 196 values corresponding to each grid cell are obtained. Thresholding is applied based on the MI values in the grid cell. Cells with MI above the threshold are considered as ferrite, while the remaining cells are considered vacuum. Each threshold corresponds to a different core structure consisting of ferrite and vacuum segments. The threshold with the corresponding reward of MIs obtained from Ansys is input to the SVR model, resulting in a threshold of 11 μH as the optimal threshold. Fig. 9 shows the results from asymmetric ferrite core structures with a threshold of 11 μH. Table IV lists the ferrite reduction and MI enhancement obtained with SVR generated core pattern shown in Fig. 9. The SVR optimized the core structure with 11.41 μH in a ferrite core pattern, corresponding to an overall ferrite reduction of 24.49% and MI increase of 0.176% compared with a conventional solid ferrite core shape.

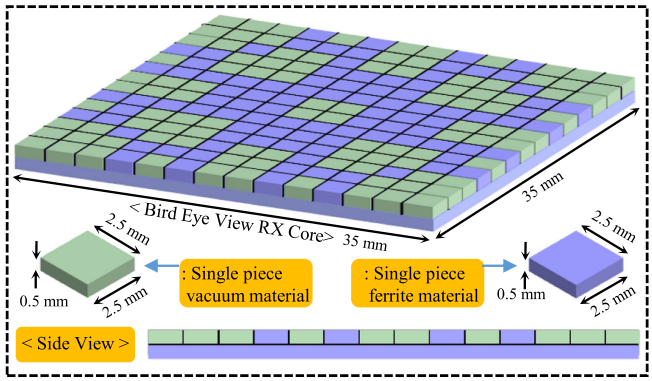

Fig. 10. Top-layer optimized core with reduced ferrite.

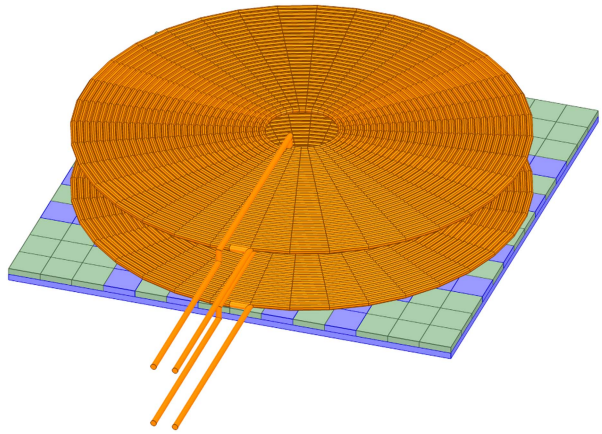

Fig. 11. Simulation setup for optimized coil and core.

C. DQN Optimization Performance

The upper layer of the ferrite core is subjected to DQN optimization for fourth- and eighth-order rotational symmetry. The fourth-order symmetric structure has both x- and y-axis symmetry, with each quadrant having 7 × 7 square patches. The 49^2 possible cases result in various ferrite core structures consisting of ferrite and vacuum patches, with the ferrite position indicated as 1 and vacuum position indicated as 0. The DQN after 100 iterations provides the core structure 4th order symmetry given in Fig. 9. The eighth-order symmetry occurs every 45° and constrains symmetry to occur in every quadrant along with the x- and y-axis symmetry with a total of 24^2 possible patterns, excluding the corner patch as vacuum. After 100 iterations, DQN provides the core structure shown in Fig. 10. The simulation setup given in Fig. 11 show the overall arrangement of Rx core,

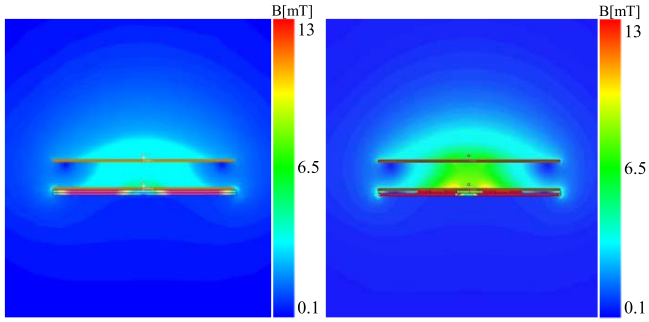

Fig. 12. Comparison of magnetic field strength. (a) Conventional core. (b) Proposed core designs.

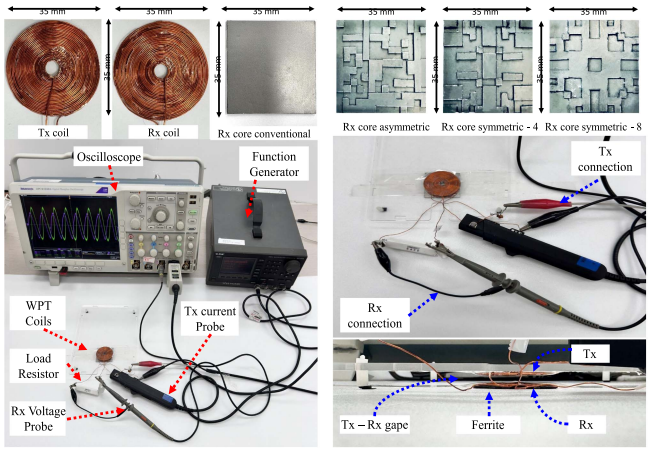

Fig. 13. Experimental setup for validating WPT design results.

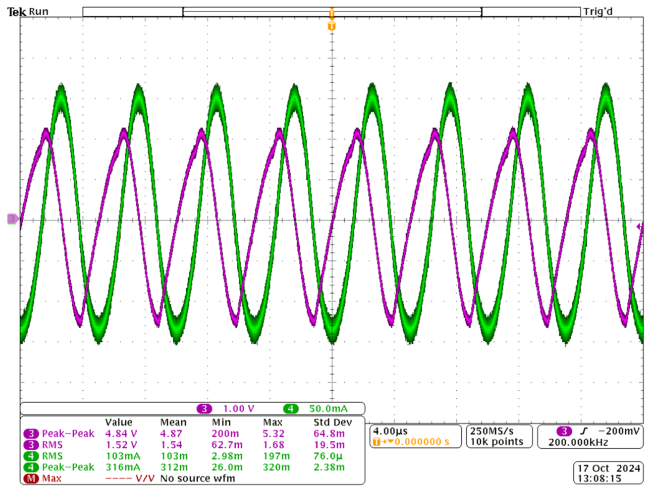

Fig. 14. Measurement results.

Rx coil, and Tx coil. Table IV lists the ferrite reduction and MI enhancement per threshold given for the pattern shown in Fig. 9. Table III shows that the fourth-order DQN symmetric structure provides 11.60 μH, which is 1.84% higher than the value provided by a conventional structure while reducing ferrite by 23.47%. Moreover, the eighth-order DQN symmetric structure provides 12.01 μH, which is 5.44% higher than the value provided by a conventional structure while reducing ferrite by 25.51%.

The impact of the proposed core design on the magnetic field distribution is illustrated in Fig. 12. A comparison of the magnetic field strength, in terms of magnitude, shows that the proposed core design achieves a B-field strength that is almost double that of the conventional core design, as shown in the legend of Fig. 12. This indicates that the proposed core structure demonstrates a stronger and more concentrated magnetic flux. This enhancement is achieved through improved flux guidance and reduced leakage in the proposed core geometry, ensuring that more magnetic energy is directed toward the intended transfer path rather than dispersing into the surrounding space. The vector plots further confirm better flux alignment and reduced fringing fields, leading to increased efficiency in WPT.

IV. Experimental Verification

The Tx and Rx windings, estimated using ML, including the asymmetric, fourth-order, and eighth-order rotationally symmetric ferrite structures, were fabricated as shown in Fig. 13. In the experimental setup, uncertainties were quantified by cross-checking the capacitance of the tuning capacitors using an RLC meter. The function generator output and oscilloscope probes were properly connected, and the oscilloscope grid was adjusted for clear visibility of the current and voltage waveforms, with both signals aligned along the zero axis. Coils and cores with minimal fabrication errors were selected for the experiment. Alignment was optimized by adjusting the positions of the ferrite, vacuum segments, and the coil relative to the core. The experimental setup, along with the dimensions of both the Tx and Rx coils, as well as the detailed measurements of the conventional, asymmetric, and symmetric fourth and eighth orders, is presented in Fig. 13. The Tx winding was tuned to a frequency of 190 kHz with a series resonant capacitor of 42 nF. The Rx winding was fixed to conventional, asymmetric, fourth-, and eighth-order symmetric ferrite structures and connected to series resonant capacitors of 26, 27, 27, and 27 nF, respectively. Both the Tx and Rx spiral planar windings with an initial radius of 2.7 mm and 30 turns were made of 0.45 mm-thick insulated round copper wire. The Tx winding is connected to the function generator, while the Rx winding is connected to a 200 Ω load. The oscilloscope probes are connected to measure the source current and load voltage, as shown in Fig. 14. The measured MIs are listed in Table IV. Due to fabrication errors, minor variations existed between the simulation and measured results. The MI was calculated as

$$M = \frac{V_{\text{rms}}}{\omega I_{\text{rms}}} \tag{17}$$

where M is the MI, V_{rms} is the induced root-mean-squared (rms) voltage across an Rx load resistor of 200 Ω, ω is the operating frequency, and I_{rms} is the rms current through the transmitting coil. The MI of the symmetric order-8 pattern is verified by measurement using an impedance analyzer, which yields a value

TABLE V
COMPARISON AND VERIFICATION OF THE SYMMETRIC ORDER 8 PATTERN RESULTS GIVEN IN FIG. 9 AND TABLE IV

Method	Ansys simulation	Impedance analyzer	Series aiding/ opposing	Experiment in (17)
MI	12.01 μH	11.77 μH	11.70 μH	11.64 μH

of 11.77 μH. In addition, the MI measured using the series-aiding and series-opposing methods is 11.7 μH. A summary of all MI measurements for the symmetric order-8 pattern is provided in Table V. The values obtained from ANSYS simulation, impedance analyzer, series-aiding and series-opposing methods, and our experiments in (17) are in close agreement.

The maximum efficiency of the proposed WPT system is determined by the magnetic coupling coefficient k and the quality factor Q. It is mathematically expressed as follows:

$$\eta_{\max} = \frac{(kQ)^2}{\left(1+\sqrt{1+(kQ)^2}\right)^2}. \tag{18}$$

In (18), the parameter k represents the magnetic coupling coefficient between the transmitting (Tx) and receiving (Rx) coils, and is defined as follows:

$$k \equiv \frac{M}{\sqrt{L_1 L_2}} \tag{19}$$

where M in (19) denotes the MI and L_1 and L_2 are the self-inductances of the Tx and Rx coils, respectively. The coupling coefficient k quantifies the magnetic link between the coils and typically ranges from 0 (no coupling) to 1 (perfect coupling). The overall quality factor Q, which reflects the combined energy efficiency of the Tx and Rx coils, is defined as follows:

$$Q \equiv \sqrt{Q_1 Q_2} \tag{20}$$

where Q_1 and Q_2 in (20) denote the individual quality factors of the Tx and Rx coils, respectively. These values are a measure of how effectively each coil stores and transfers energy, and can be approximated by

$$Q_{1,2} \approx \frac{\omega_0 L_{1,2}}{R_{\text{ac}1,2}}. \tag{21}$$

In (21), ω_0 is the operating angular frequency, $L_{1,2}$ is the inductance of the corresponding coil, and $R_{\text{ac}1,2}$ denotes its effective ac resistance at the operating frequency. Higher values of Q and k correspond to improved system efficiency. The series-compensated circuit used in the experimental setup of the proposed WPT system is shown in Fig. 18. The circuit was tested with various load resistances R_L, as summarized in Table VI. Among the tested values, the optimal load was identified as $R_L = 25.5\ \Omega$, at which the maximum PTE of 96.5% was achieved. The peak-to-peak source voltage and current, along with the peak-to-peak load voltage corresponding to this optimal load, are illustrated in Fig. 16. For comparison, load values of $R_L = 20\ \Omega$ and $R_L = 27\ \Omega$ yielded lower PTE, as shown in Figs. 15 and 17, respectively, and further detailed in Table VI.

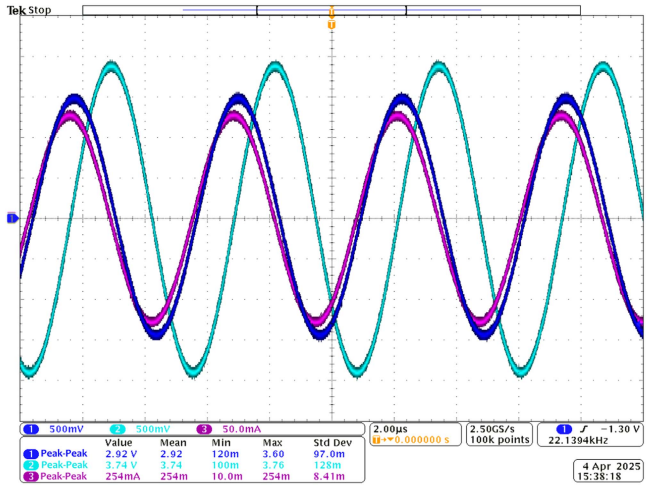

Fig. 15. Measurement results for a 20 Ω load resistor with both Tx and Rx coils tuned to 190 kHz.

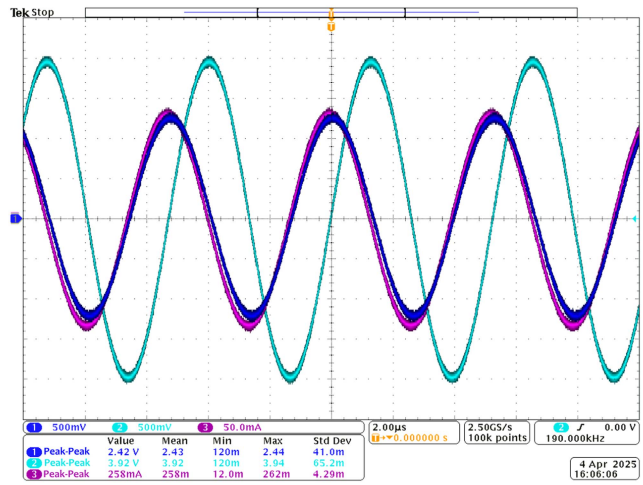

Fig. 16. Measurement results for a 25.5 Ω load resistor with both Tx and Rx coils tuned to 190 kHz.

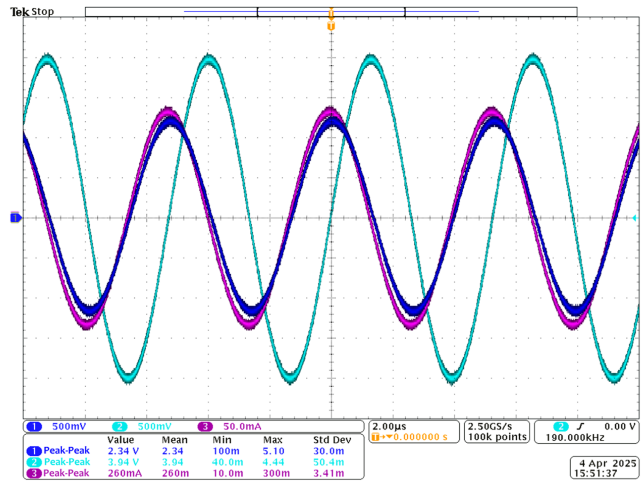

Fig. 17. Measurement results for a 27.0 Ω load resistor with both Tx and Rx coils tuned to 190 kHz.

TABLE VI
PTE OF THE PROPOSED WPT SYSTEM AT VARIOUS LOAD RESISTANCES

P_s	V_{rms}	R_L	P_o	η
0.109	1.237	15.00	0.102	93.7%
0.093	1.322	20.00	0.087	94.3%
0.080	1.379	25.00	0.076	95.1%
0.078	1.386	25.50	0.075	96.5%
0.078	1.393	26.00	0.075	95.7%
0.076	1.393	27.00	0.072	94.5%

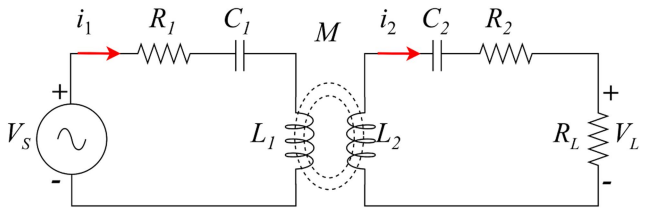

Fig. 18. Circuit diagram of the proposed WPT system where $R_1 = 2.56\ \Omega$, $R_2 = 1.35\ \Omega$, $R_L = 25.5\ \Omega$, $C_1 = 37.7$ nF, $C_2 = 33.3$ nF, $L_1 = 16.3\ \mu$H, $L_2 = 21.2\ \mu$H, and $M = 11.7\ \mu$H.

V. CONCLUSION

We demonstrate the effectiveness of ML in optimizing WPT systems for electroceuticals. Traditional design methods fail to suitably handle magnetic field nonlinearities, making them less effective for inductive power transfer components. By employing a hybrid ML framework with SVR-based multivariate regression and DQN models, we achieve substantial improvements in coil winding and ferrite core designs. The optimized winding structure achieves an MI of 11.284 μH with a conventional solid ferrite core. Further, SVR optimization increases the MI by 0.585% while reducing the ferrite volume by 24.49%. DQN models for rotationally symmetric core designs improve the MI by 1.382% and 3.1554% while also reducing ferrite volume. Overall, our ML-based design framework efficiently optimizes WPT systems, enhancing their performance and material efficiency, being promising for advanced electroceutical applications.

REFERENCES

[1] C. Han, J. Mao, S. Yu, and Z. Zhang, "An investigation of implantable capacitive coupling intra-body power transfer based on full-band loss compensation," *IEEE Trans. Power Electron.*, vol. 39, no. 7, pp. 8904–8915, Jul. 2024.

[2] M. Li, A. Khaleghi, A. Hasanvand, R. P. Narayanan, and I. Balasingham, "A new design and analysis for metasurface-based near-field magnetic wireless power transfer for deep implants," *IEEE Trans. Power Electron.*, vol. 39, no. 5, pp. 6442–6454, May 2024.

[3] I. A. Shah, Y. Cho, and H. Yoo, "Safety evaluation of medical implants in the human body for a wireless power transfer system in an electric vehicle," *IEEE Trans. Electromagn. Compat.*, vol. 63, no. 3, pp. 681–691, Jun. 2021.

[4] S. Roy, A. W. Azad, S. Baidya, M. K. Alam, and F. Khan, "Powering solutions for biomedical sensors and implants inside the human body: A comprehensive review on energy harvesting units, energy storage, and wireless power transfer techniques," *IEEE Trans. Power Electron.*, vol. 37, no. 10, pp. 12237–12263, Oct. 2022.

[5] X. Du, C. Li, and D. Dujić, "Design and characterization of PCB spiral coils for inductive power transfer in medium-voltage applications," *IEEE Trans. Power Electron.*, vol. 37, no. 5, pp. 6168–6180, May 2022.

[6] B.-G. Choi and Y.-S. Kim, "New structure design of ferrite cores for wireless electric vehicle charging by machine learning," *IEEE Trans. Ind. Electron.*, vol. 68, no. 12, pp. 12162–12172, Dec. 2021.

[7] A. Basir, I. A. Shah, and H. Yoo, "Sphere-shaped receiver coil for misalignment-resilient wireless power transfer systems for implantable devices," *IEEE Trans. Antennas Propag.*, vol. 70, no. 9, pp. 8368–8378, Sep. 2022.

[8] J. Rahulkumar and R. Narayanamoorthi, "Delta and inverse delta coupler optimization using machine learning for wireless power transfer electric vehicle charging application," *IEEE Trans. Power Electron.*, vol. 40, no. 1, pp. 2556–2568, Jan. 2025.

[9] P. Leszczynski, K. Kutorasinski, M. Szewczyk, and J. Pawłowski, "Machine-learned models for power magnetic material characteristics," *IEEE Trans. Power Electron.*, vol. 40, no. 1, pp. 1554–1562, Jan. 2025.

[10] L. Alzubaidi et al., "Review of deep learning: Concepts, cnn architectures, challenges, applications, future directions," *J. big Data*, vol. 8, pp. 1–74, 2021.

[11] A. A. Hasnain, A. Basir, Y. Cho, I. A. Shah, and H. Yoo, "RSS-based machine-learning-assisted localization and tracking of a wireless capsule endoscope," *IEEE Trans. Instrum. Meas.*, vol. 73, 2024, Art. no. 4011811.

[12] C. Lin, J. Xu, J. Hou, Y. Liang, and X. Mei, "Ensemble method with heterogeneous models for battery state-of-health estimation," *IEEE Trans. Ind. Informat.*, vol. 19, no. 10, pp. 10160–10169, Oct. 2023.

[13] D. Sarkar, T. Khan, F. A. Talukdar, and S. R. Rengarajan, "Computational intelligence for modeling and optimization of RFEH and WPT systems: A comprehensive survey: Computational intelligence for RFEH and WPT systems," *IEEE Microw. Mag.*, vol. 24, no. 9, pp. 46–60, Sep. 2023.

[14] A. Ali, M. N. Mohd Yasin, M. Jusoh, N. A. M. A. Hambali, and S. R. A. Rahim, "Optimization of wireless power transfer using artificial neural network: A review," *Microw. Opt. Technol. Lett.*, vol. 62, no. 2, pp. 651–659, 2020.

[15] S. Shimokawa et al., "Fast 3-D optimization of magnetic cores for loss and volume reduction," *IEEE Trans. Magn.*, vol. 54, no. 11, pp. 1–4, Nov. 2018.

[16] K. Pretorius and N. Pillay, "Neural network crossover in genetic algorithms using genetic programming," *Genet. Programm. Evolvable Machines*, vol. 25, no. 1, pp. 1–30, 2024.

[17] B.-G. Choi, E. S. Lee, and Y.-S. Kim, "Optimal structure design of ferromagnetic cores in wireless power transfer by reinforcement learning," *IEEE Access*, vol. 8, pp. 179295–179306, 2020.

[18] M. S. Jeong, J. H. Jang, and E. S. Lee, "Optimal IPT core design for wireless electric vehicles by reinforcement learning," *IEEE Trans. Power Electron.*, vol. 38, no. 11, pp. 13262–13272, Nov. 2023.

[19] P. Dixit and S. Silakari, "Deep learning algorithms for cybersecurity applications: A technological and status review," *Comput. Sci. Rev.*, vol. 39, 2021, Art. no. 100317.

[20] R. Vinayakumar, M. Alazab, K. Soman, P. Poornachandran, A. Al-Nemrat, and S. Venkatraman, "Deep learning approach for intelligent intrusion detection system," *IEEE Access*, vol. 7, pp. 41525–41550, 2019.

[21] G. Liu, H. Bao, and B. Han, "A stacked autoencoder-based deep neural network for achieving gearbox fault diagnosis," *Math. Problems Eng.*, vol. 2018, pp. 1–10, 2018.

[22] K. Alrawashdeh and C. Purdy, "Fast hardware assisted online learning using unsupervised deep learning structure for anomaly detection," in *Proc. 2018 Int. Conf. Inf. Comput. Technol.*, 2018, pp. 128–134.

[23] T. Young, D. Hazarika, S. Poria, and E. Cambria, "Recent trends in deep learning based natural language processing," *IEEE Comput. Intell. Mag.*, vol. 13, no. 3, pp. 55–75, Aug. 2018.

[24] Y. Hao, Q. Lu, X. Wang, and B. Jiang, "Adaptive model-based reinforcement learning for fast-charging optimization of lithium-ion batteries," *IEEE Trans. Ind. Informat.*, vol. 20, no. 1, pp. 127–137, Jan. 2024.

[25] J. Fang, L. Zheng, C. Liu, and C. Su, "A data-driven case generation model for transient stability assessment using generative adversarial networks," *IEEE Trans. Ind. Informat.*, vol. 20, no. 12, pp. 14391–14400, Dec. 2024.

[26] Z. He and F. Tong, "Residual RNN models with pruning for digital predistortion of RF power amplifiers," *IEEE Trans. Veh. Technol.*, vol. 71, no. 9, pp. 9735–9750, Sep. 2022.

[27] X. Tian, K. T. Chau, W. Liu, H. Pang, and C. H. Lee, "Maximum power tracking for magnetic field editing-based omnidirectional wireless power transfer," *IEEE Trans. Power Electron.*, vol. 37, no. 10, pp. 12901–12912, Oct. 2022.

[28] Y. Li et al., "A novel hybrid magnetic core design method for weight reduction of wireless power transfer systems," in *Proc. IEEE Appl. Power Electron. Conf. Expo.*, 2024, pp. 1202–1206.

Fawad received the Ph.D. degree in telecommunication engineering from the University of Engineering and Technology, Taxila, Pakistan, in 2021.

Since October 2023, he has been a Postdoctoral Fellow with Power System Laboratory, Gwangju Institute of Science and Technology, Gwangju, South Korea. From 2022 to 2023, he was a Postdoctoral Researcher with the College of Dentistry, Chosun University, Gwangju, South Korea. His research interests include medical image diagnostics, pattern recognition, deep learning, machine learning, image processing, computer vision, and wireless communication.

Syed Ahson Ali Shah (Member, IEEE) received the B.Sc. degree in telecommunication engineering from the University of Engineering and Technology, Mardan, Pakistan, in 2015, and the Ph.D. degree in electronic engineering from Hanyang University, Seoul, South Korea, in 2022.

He was a Postdoctoral Researcher with Hanyang University until 2023, and since then with Gwangju Institute of Science and Technology, Gwangju, South Korea. To date, he has authored or coauthored several journal articles and conference papers. His research interests include antennas and RF systems, implant safety, wireless power transfer, biotelemetric stents, metamaterials, 5G antennas, and magnetic field focusing, circuit modeling, and TMS coils.

Dr. Shah was the recipient of IETE MN SAHA Memorial Award and Gold Medal for best Application-Oriented Paper, in 2018, Bronze Paper Award at IEEE Student Paper Contest, Seoul, in 2019, 2021, 2022, and 2024, and the 3rd Best Student Paper Award in 2021 Competition arranged by the Korean Institute of Electromagnetic Engineering and Science (KIEES). His Ph.D. Thesis has been recognized as one of the excellent dissertations and was the recipient of the Best Ph.D. Thesis Award in overall university and the only in Electronic Engineering Department. He is also a Reviewer for Nature, Wiley, MDPI, and IEEE Transactions and Journal. He is the Associate Editor for *JMIR Biomedical Engineering Journal*, Academic Editor for *Hindawi*, Guest Editor for *MDPI* and *PLoS One*.

Yohan Park (Student Member, IEEE) received the B.S. degree in electronic engineering from Chonnam National University, Gwangju, South Korea, in 2021. He is currently working toward the Ph.D. degree with the Department of Electrical Engineering and Computer Science, Gwangju Institute of Science and Technology, Gwangju, Korea.

His research interests include distribution network, distributed energy resources, distribution network state estimation, and wireless power transfer.

Yun-Su Kim (Senior Member, IEEE) received the B.S. and Ph.D. degrees in electrical engineering from Seoul National University, Seoul, South Korea, in 2010 and 2016, respectively.

from 2015 to 2017, he was a Senior Researcher with Korea Electrotechnology Research Institute. He joined the Faculty of the Gwangju Institute of Science and Technology (GIST) in 2018, where he is currently a Professor with the Department of Electrical Engineering and Computer Science. From 2023 to 2024, he was a Fulbright Visiting Scholar with the University of Hawai'i at Mānoa, School of Law, Honolulu, HI, USA. His research interests include distribution network, energy management system, optimal bidding strategy, microgrid, and wireless power transfer.

Dr. Kim is an Associate Editor for IEEE TRANSACTIONS ON SUSTAINABLE ENERGY since 2023. He was a Director of the Korean Society for New and Renewable Energy and the Korean Institute of Electrical Engineers.